

Unlocking Generalization Power in LiDAR Point Cloud Registration

Zhenxuan Zeng^{1,2}, Qiao Wu^{1,2}, Xiyu Zhang^{1,2}, Lin Yuanbo Wu³, Pei An⁴
 Jiaqi Yang^{1,2*}, Ji Wang^{1,2*}, Peng Wang^{1,2}

¹School of Computer Science, Northwestern Polytechnical University, China.

²Ningbo Institute, Northwestern Polytechnical University, China.

³Department of Computer Science, Swansea University, United Kingdom.

⁴HuaZhong University of Science and Technology, China.

{zengzhenxuan, qiaowu}@mail.nwpu.edu.cn {jqyang, j.wang, peng.wang}@nwpu.edu.cn

Abstract

In real-world environments, a LiDAR point cloud registration method with robust generalization capabilities (across varying distances and datasets) is crucial for ensuring safety in autonomous driving and other LiDAR-based applications. However, current methods fall short in achieving this level of generalization. To address these limitations, we propose UGP, a pruned framework designed to enhance generalization power for LiDAR point cloud registration. The core insight in UGP is the elimination of cross-attention mechanisms to improve generalization, allowing the network to concentrate on intra-frame feature extraction. Additionally, we introduce a progressive self-attention module to reduce ambiguity in large-scale scenes and integrate Bird’s Eye View (BEV) features to incorporate semantic information about scene elements. Together, these enhancements significantly boost the network’s generalization performance. We validated our approach through various generalization experiments in multiple outdoor scenes. In cross-distance generalization experiments on KITTI and nuScenes, UGP achieved state-of-the-art mean Registration Recall rates of 94.5% and 91.4%, respectively. In cross-dataset generalization from nuScenes to KITTI, UGP achieved a state-of-the-art mean Registration Recall of 90.9%. Code will be available at <https://github.com/peakpang/UGP>

1. Introduction

LiDAR point cloud registration is essential in applications such as autonomous driving [14] and SLAM [24, 25, 29]. The dynamic nature of LiDAR scenes often necessitates pairwise registration of point clouds that exhibit 1) cross-distance variations (e.g., point clouds captured at different

*Corresponding author

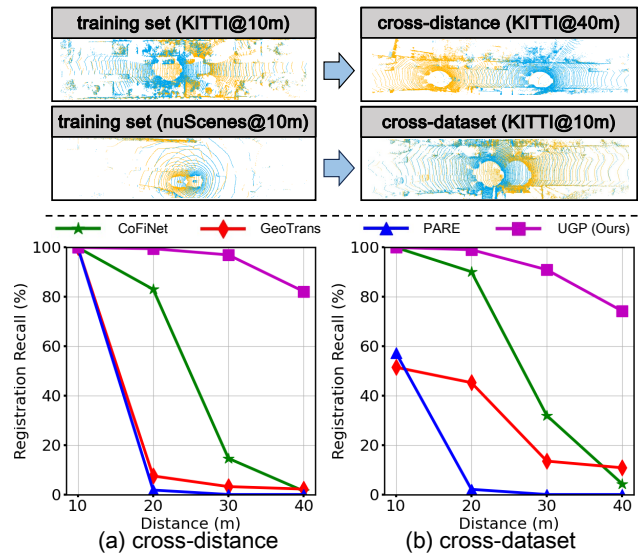


Figure 1. Illustration of the generalization performance of leading methods [28, 38, 39] in cross-distance and cross-dataset. (a) Cross-distance generalization: train on KITTI@10m, test on KITTI@40m. (b) Cross-dataset generalization: train on nuScenes@10m [4], test on KITTI@10m. These methods experience substantial performance degradation due to poor generalization. In contrast, our method achieves the best registration results on both cross-distance and cross-dataset.

speeds or times) and 2) cross-dataset variations (e.g., point clouds collected in distinct environments). To tackle these real-world challenges, this research seeks to develop a LiDAR point cloud registration framework that can effectively generalize across both cross-distance and cross-dataset variations.

Recently, learning-based methods for point cloud registration have gained prominence [1, 3, 5, 9, 13, 16, 27, 40]. However, most of these methods focus on enhancing per-

formance under same-distance or same-dataset conditions, with only a few addressing cross-dataset generalization. Notably, SpinNet [1] and BUFFER [2] use patch-wise feature extraction, which provides robustness against noise and occlusion. Nonetheless, to our knowledge, none of existing methods has systematically investigated generalization performance for LiDAR point cloud registration. Unlike evenly distributed indoor RGB-D point clouds, LiDAR point clouds exhibit uneven distribution where the point density decreases significantly as the distance from the sensor increases. This introduces unique challenges: 1) cross-distance variations alter the overlap rate between point cloud pairs and cause density changes within the overlap region, and 2) cross-dataset variations lead to differences in data characteristics (*e.g.*, 64-line vs. 32-line LiDAR) and feature distributions (*e.g.*, environmental shifts). We observe that state-of-the-art (SOTA) methods suffer noticeable performance degradation under both cross-distance and cross-dataset conditions. As shown in Fig. 1, CoFiNet [39], GeoTrans [28], and PARE [38] are coarse-to-fine methods that use the transformer to improve registration performance under the same distance or same dataset conditions. Among these approaches, cross-attention is extensively used to model the geometric consistency across the two point clouds. However, the effectiveness of this module relies on an implicit assumption: *consistency in the representation of the same structure across the two point clouds*. In dynamic scenarios where cross-distance and cross-dataset generalization challenges arise, this implicit assumption often does not hold due to the inconsistent density distribution of LiDAR point clouds.

To tackle these challenges, we propose a LiDAR point cloud registration framework with strong generalization power (**UGP**). The framework’s key insight is eliminating the cross-attention module to **Unlock Generalization Power** and enable the network to focus on intra-frame feature extraction. First, to reduce the impact of inconsistent geometric representations in inter-frame, we eliminate the cross-attention module. This encourages the network to concentrate on intra-frame spatial information. Second, to reduce feature ambiguity in LiDAR scenes and capture finer local feature associations, we introduce a progressive self-attention module. This module gradually increases the attention range of superpoints, enabling them to prioritize local spatial information and construct a multi-scale spatial representation. Lastly, recognizing the importance of scene-element-level (*e.g.*, roads, corners) semantic information in reducing scene ambiguity, we incorporate Bird Eye View (BEV) features to improve accuracy during the coarse matching stage. In summary, our main contributions are as follows:

- We reveal that inconsistent geometric representations in LiDAR scenarios cause the cross-attention module to

limit network generalization capability. An effective way to unlock this is to eliminate the cross-attention module.

- We also propose a progressive self-attention module and a BEV feature extraction module to more effectively focus on fine local space associations and capture semantically rich information, reducing ambiguity in point clouds and enhancing generalization.
- In cross-distance generalization from 10m to 40m, UGP achieved 82.0% (+20.8%) registration recall (RR) on KITTI and 72.3% (+57.1%) RR on nuScenes, outperforming BUFFER [2]. In cross-dataset generalization from nuScenes to KITTI, our method achieved a state-of-the-art mean RR of 90.9% (+6.2%) over BUFFER [2].

2. Related Work

Learning-based Point Cloud Registration. Learning-based point cloud registration methods have become a powerful approach for aligning point clouds. Current methods often employ a coarse-to-fine strategy [6, 23, 28, 34, 38–41], which loosens the constraints of strict point-to-point matching in favor of patch-level matching. This approach reduces repeatability requirements, significantly enhancing registration accuracy. However, these methods rely heavily on the data distribution of training point cloud pairs, which limits their generalization capability. Following this line, point-wise methods [3, 8] utilize architectures such as Minkowski [7] and KPConv [32] to extract dense point features, while patch-wise methods [1, 2, 9, 13, 27] capture features from the local regions around key points through carefully designed networks. The robustness of local patches to noise and occlusion gives these patch-based approaches a promising generalization potential. Recent studies [18–20] have focused on point cloud registration across varying distances. However, these approaches rely solely on visible full-range data and require carefully designed multi-frame training to ensure registration performance within the visible range.

Point Cloud Registration with Transformers. The Transformer architecture [33] introduced an attention mechanism that captures global dependencies and has been widely used for point cloud registration. For example, CoFiNet [39] uses vanilla attention mechanism to establish global geometric consistency, while GeoTrans [28] integrates geometric structure to enhance feature robustness. PEAL [41] employs one-way attention with overlap priors to reduce ambiguity from non-overlapping points. DCATr [6] limits attention to specific cues to minimize irrelevant interference. Unlike these methods, we propose a progressive self-attention mechanism that gradually expands the spatial attention range, prioritizing finer local spatial structure associations, reducing ambiguity in large scenes, and improving registration accuracy.

Multi-modal Point Cloud Registration. Incorporating

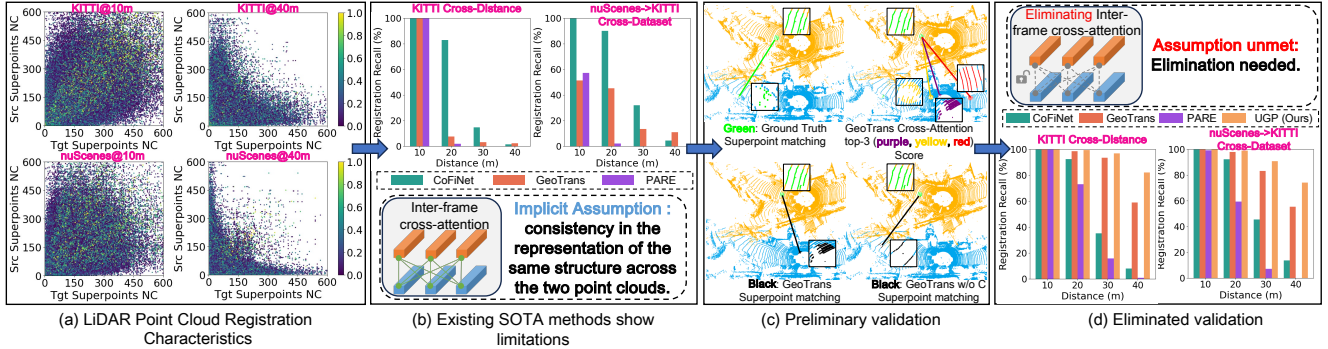


Figure 2. **Motivation.** We conducted a statistical analysis of the matching characteristics in LiDAR scenes and identified the limitations of existing methods. This was followed by preliminary visualizations and elimination experiments to validate our findings. (a) Each point in the figure represents a ground truth corresponding superpoint pair. The position of each point indicates the neighborhood count (NC) of the superpoint within a radius of $r = 2.4m$ in both the source (src) and target (tgt) point clouds, and the color represents the overlap degree of the corresponding superpoint pairs after rotation by the ground truth transformation. (b) Performance of existing methods in cross-distance (upper left) and cross-dataset (upper right). (c) GeoTrans [28] cannot match superpoints (cross-distance, from KITTI@10m to KITTI@20m). (d) The performance of existing methods after eliminating cross-attention, and UGP (ours).

multi-modal information for point cloud understanding has gained significant traction in recent research. For example, RPVNet [35] enhances segmentation accuracy by integrating the range image modality. Methods such as BYOC [10], PCRCG [43], and IGRReg [36] fuse image features with point clouds to support registration tasks. Similarly, PEAL2D [41] utilizes a 2D image to derive an overlap prior, aiding in point cloud registration. BEV images, widely adopted in 3D object detection [37] and place recognition [22], are particularly effective due to their clear global edge features. To enhance matching accuracy in the coarse stage, we explicitly incorporate BEV images into point cloud registration.

3. Motivation

In real-world dynamic scenarios, we face the challenge of registering point clouds with 1) cross-distance variations (*e.g.*, point clouds captured at different speeds or times) and 2) cross-dataset variations (*e.g.*, point clouds collected in distinct environments or using different LiDAR types). This challenge requires the LiDAR point cloud registration framework to possess cross-distance and cross-dataset generalization power. To address this, we analyze the matching characteristics under both challenges and find that existing methods have limited performance. Finally, we propose targeted improvements that effectively address these existing challenges.

a) Inherent Challenges with LiDAR Point Cloud Registration. Fig. 2 (a) highlights the challenges in LiDAR point cloud registration by visualizing data distributions of ground truth matching point pairs across varying distances and datasets. 1) At closer distances (*e.g.*, KITTI@10m or

nuScenes@10m), there is a high number of matched pairs with consistent density (clustered near $y = x$) and a high overlap score. As the distance increases (*e.g.*, KITTI@40m vs. KITTI@10m or nuScenes@40m vs. nuScenes@10m), the proportion of pairs with inconsistent density grows. Additionally, increased distance brings changes in perspective and occlusion, reducing overlap rates even among points with similar density. 2) Cross-dataset comparisons reveal differences in data characteristics, such as the shift from nuScenes (32-line LiDAR) to KITTI (64-line LiDAR).

b) Implicit Assumption of Cross-Attention Based Methods. The effectiveness of SOTA methods such as CoFiNet [39], GeoTrans [28], and PARE [38] relies on an implicit assumption: *consistency in the representation of the same structure across two point clouds*. However, cross-attention cannot adapt to variations in the consistency representation of the same structure across different distances and datasets, limiting the network’s generalization performance, as shown in Fig. 2 (b).

c) Cross-Attention Elimination. To demonstrate the limitations of cross-attention, we present results from GeoTrans [28] trained on KITTI@10m and tested on KITTI@20m, as shown in Fig. 2 (c). First, we show a challenging superpoint matching example on the ground, where uneven LiDAR distribution and limited geometric detail make accurate matching difficult. As the distance between point cloud pairs increases (*e.g.*, green ground-truth matches at 20m), variations in density and occlusion worsen matching accuracy. Cross-attention-based methods like GeoTrans [28], fail in cross-distance matching by relying on density-similar but incorrect matches. Visualization of GeoTrans [28]’s top-3 score areas from its final cross-attention layer shows that it primarily captures similarly

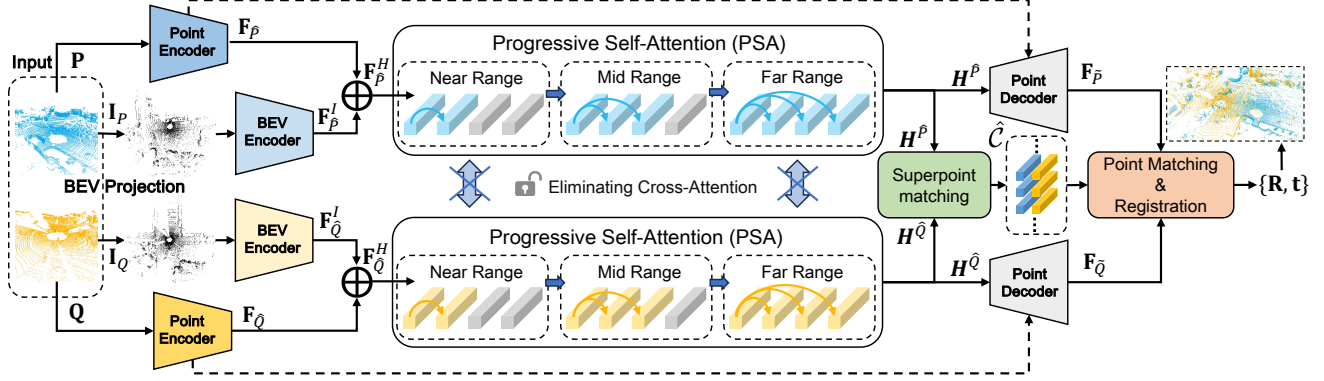


Figure 3. **Overview of UGP.** The input point cloud is first projected to obtain the corresponding BEV image. Then, the point cloud and BEV image are fed into the Point Encoder and BEV encoder, respectively, for downsampling and feature extraction. In the superpoint matching stage, the indexing relationship between superpoints and BEV is used to fuse point-level features and image features. The fused features are used as input to the progressive self-attention module to extract robust and consistent intra-frame features. Finally, the superpoint matching results are propagated to dense points for dense matching, enabling the recovery of the rigid transformation.

dense structures and struggles to adapt to shifts in data distribution, resulting in outlier matches. By eliminating cross-attention, superpoint matching refocuses on correct areas near the ground truth. Preliminary validation followed by elimination experiments (Fig. 2 (d)) confirms that eliminating cross-attention greatly enhances model generalization.

d) Boosting the Robustness and Consistency of Intra-Frame Feature Learning. After eliminating the cross-attention module, we encourage the network to concentrate on intra-frame spatial information. A vanilla self-attention [33] forces each point to interact with all other points equally. However, this leads to feature ambiguity due to irrelevant distant points. To improve the robustness and consistency of intra-frame feature extraction, we propose a progressive self-attention. In the initial layer, the attention range is restricted to the local space, preserving fine-grained local information. In subsequent layers, the attention range is gradually expanded to incorporate the global context. This progressive approach reduces feature ambiguity and enhances the model’s ability to effectively capture both local and global structure. Besides, point-based backbones such as KPConv [32] are difficult to establish a association between local geometric structures and global background information [21, 35]. This further worsens the ambiguity of the features. To this end, we introduce BEV which can provide additional semantic information of scene elements (*e.g.*, roads, corners) to the local geometric features extracted by KPConv.

4. Method

Given two sets of partially overlapped point clouds $\mathbf{P} \in \mathbb{R}^{N \times 3}$ and $\mathbf{Q} \in \mathbb{R}^{M \times 3}$, our objective is to recover the optimal rigid transformation between them, denoted as $\mathbf{T} = \{\mathbf{R} \in SO(3), \mathbf{t} \in \mathbb{R}^3\}$, where \mathbf{R} represents rotation and \mathbf{t}

represents translation. As illustrated in Fig. 3, we adopt a coarse-to-fine strategy and eliminate the cross-attention module. First, the point cloud is directly projected to obtain the BEV image (Sec. 4.1). Then, the Point-Encoder and BEV-Encoder are used to extract the scale features of the point cloud and BEV image. Next, the patch features of the point cloud and image are fused to obtain the superpoint features (Sec. 4.2). The superpoint matching module eliminates the cross-attention module and utilizes only the progressive self-attention to extract superpoint features, thereby obtaining superpoint correspondences (Sec. 4.3). Finally, we follow GeoTransformer [28], using the same point matching module to refine the superpoint matching and recover the alignment transformations with the LGR [28] approach (Appendix Sec. 7).

4.1. BEV Projection

In LiDAR point cloud registration, the significant global edge and texture feature are important for superpoint matching. From a 2D perspective, the BEV representation of the point cloud provides a global view of the environment and offers important semantic information about scene elements. These prominent features reduce the ambiguity of the scene and improve feature consistency.

Given a point cloud $\mathbf{P} = \{(x_i, y_i, z_i) \mid i = 1, 2, \dots, N\}$, where (x_i, y_i, z_i) represents the coordinates of each point, we project into a BEV image $\mathbf{I} \in \mathbb{R}^{H \times W}$, where H and W denote the height and width of the BEV image, respectively. Assuming that the ground area covered by this aerial view is $[x_{\min}, x_{\max}]$ and $[y_{\min}, y_{\max}]$, the projection process can be expressed by the following formula :

$$u_i = \left\lfloor \frac{x_i - x_{\min}}{x_{\max} - x_{\min}} \cdot H \right\rfloor, v_i = \left\lfloor \frac{y_i - y_{\min}}{y_{\max} - y_{\min}} \cdot W \right\rfloor, \quad (1)$$

where (u_i, v_i) is the pixel coordinate of point (x_i, y_i, z_i) in

the BEV image. To capture the global structure, we fill each pixel position with a gray value of $\mathbf{I}(u_i, v_i) = 1$.

4.2. Superpoint Feature Extraction and Fusion

Our feature extraction module consists of a Point-Encoder and a BEV-Encoder. The Point-Encoder employs a multi-level KPConv structure [32], with voxel downsampling applied at each layer to decrease the number of points and ultimately extract superpoint features. The BEV-Encoder uses a multi-level ResNet structure [15], applying 2D max pooling at each layer to downsample the image and extract patch-level features. Finally, we fuse the two features to obtain richer superpoints feature expressions.

Specifically, given the input point clouds \mathbf{P} and \mathbf{Q} , along with their corresponding BEV images \mathbf{I}_P and \mathbf{I}_Q , the Point-Encoder outputs the downsampled superpoints $\hat{\mathbf{P}}$ and $\hat{\mathbf{Q}}$, as well as their corresponding features $\mathbf{F}_{\hat{\mathbf{P}}} \in \mathbb{R}^{\hat{n} \times \hat{d}}$ and $\mathbf{F}_{\hat{\mathbf{Q}}} \in \mathbb{R}^{\hat{m} \times \hat{d}}$, where \hat{d} denotes the feature dimension of each superpoint. At the same time, the BEV-Encoder generates the patch features $\mathbf{F}_P^I \in \mathbb{R}^{H' \times W' \times d'}$ and $\mathbf{F}_Q^I \in \mathbb{R}^{H' \times W' \times d'}$, where H' and W' represent the height and width of the downsampled BEV image, and d' denotes the feature dimension for each patch in the BEV image. Afterwards, feature fusion is performed based on the indexing relationship between superpoints and BEV patches, where the features are concatenated to combine 3D geometry and 2D texture information. This results in the fused features $\mathbf{F}_{\hat{\mathbf{P}}}^H$ and $\mathbf{F}_{\hat{\mathbf{Q}}}^H$ for the superpoints $\hat{\mathbf{P}}$ and $\hat{\mathbf{Q}}$, respectively.

4.3. Superpoint Matching Module

For the coarse-to-fine method, superpoint matching accuracy directly determines final registration performance.

Eliminating Cross-Attention to Concentrate on Intra-Frame Feature Learning. The distributional characteristics of LiDAR data differ from indoor RGB-D point clouds, causing inconsistencies in geometric representations across distances and datasets and limiting network generalization. To improve the framework’s generalization performance, we adopt a simple, effective approach based on the observations in Sec. 3: Eliminating the cross-attention module and retaining self-attention to focus on intra-frame feature extraction, enhancing generalization.

In the following, we describe the process for computing the feature for superpoint $\hat{\mathbf{P}}$ with self-attention, which similarly applies to $\hat{\mathbf{Q}}$. Given the input feature matrix $\mathbf{X} \in \mathbb{R}^{\hat{n} \times d_t}$, where d_t represents the dimension of each input feature, the output feature matrix $\mathbf{Z} \in \mathbb{R}^{\hat{n} \times d_t}$ is obtained as the weighted sum of the projected input features:

$$\mathbf{z}_i = \sum_{j=1}^{\hat{n}} a_{i,j} (\mathbf{x}_j \mathbf{W}^V), \quad (2)$$

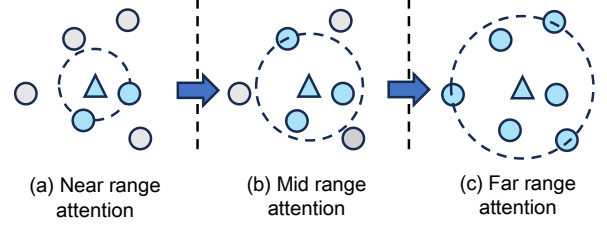


Figure 4. Illustration of our proposed progressive self-attention. In the initial layer, the triangular points prioritize attention to the local space around them, and the attention range is gradually expanded in subsequent layers

where the attention weights $a_{i,j}$ are obtained by applying a row-wise softmax to the attention scores $e_{i,j}$, and the attention scores $e_{i,j}$ computed as:

$$e_{i,j} = \frac{(\mathbf{x}_i \mathbf{W}^Q) (\mathbf{x}_j \mathbf{W}^K + \mathbf{r}_{i,j} \mathbf{W}^R)^T}{\sqrt{d_t}}. \quad (3)$$

Here, $\mathbf{r}_{i,j}$ refers to the geometric structure embedding proposed in GeoTransformer [28]. The terms $\mathbf{W}^Q, \mathbf{W}^K, \mathbf{W}^V, \mathbf{W}^R \in \mathbb{R}^{d_t \times d_t}$ are the respective projection matrices for queries, keys, values and geometric structure embeddings.

Progressive Self-Attention Module. In real-world scenarios, local contextual information plays a crucial role in point cloud feature extraction. Existing methods [6, 28, 38, 39, 41] apply global self-attention directly to the input point cloud features. Although self-attention can capture long-range global dependencies, this approach is more susceptible to noise in large-scale scenes, which aggravates the ambiguity in feature matching. To reduce the matching ambiguity in LiDAR scenes, we introduce a progressive self-attention module, as shown in Fig. 4. This module dynamically adjusts the attention range in a progressive manner, based on the distances between each point and other points in the global context. In the initial layer ($L = 1$), the module targets local association refinement by focusing on nearby superpoints, effectively reducing the ambiguity that can arise from initial global attention. In subsequent layers ($L > 1$), the attention range is gradually expanded, enabling the model to build multi-scale spatial representations of superpoints. This stepwise approach enhances the robustness of superpoint features.

Next, we will detail the computation process for $\hat{\mathbf{P}}$ at layer $L = k$, which similarly applies to $\hat{\mathbf{Q}}$. To implement progressive, the masked attention scores $e_{i,j}^{(L=k)}$ are computed as:

$$e_{i,j}^{(L=k)} = \mathbf{M}_{i,j}^{(L=k)} \cdot e_{i,j}, \quad (4)$$

where $\mathbf{M}_{i,j}^{(L=k)}$ is a layer-specific mask designed to filter attention scores based on the Euclidean distance between

Model	Train on KITTI@10m					KITTI@20m					KITTI@30m					KITTI@40m					mRR
	RRE	RTE	RRE*	RTE*	RR	RRE	RTE	RRE*	RTE*	RR	RRE	RTE	RRE*	RTE*	RR	RRE	RTE	RRE*	RTE*	RR	
FCGF [8]	0.213	<u>0.064</u>	0.864	0.185	<u>98.9</u>	0.358	0.121	5.812	1.477	92.1	1.051	0.339	11.706	10.514	64.1	1.477	0.767	19.855	30.598	18.7	68.5
SpinNet [11]	0.515	0.104	0.948	0.322	97.7	1.436	0.237	9.418	7.833	58.0	2.018	0.638	22.107	28.821	1.1	–	–	23.191	39.544	0.0	39.2
Predator [16]	0.282	0.070	0.282	0.076	99.8	1.602	0.324	16.438	12.403	30.2	1.903	0.419	28.594	28.054	1.1	–	–	30.605	38.637	0.0	32.8
CoFiNet [39]	0.344	0.083	0.357	0.089	99.8	1.133	0.256	3.758	2.924	82.9	1.862	0.557	18.521	24.992	14.6	2.054	0.807	25.716	39.071	1.4	49.7
GeoTrans [28]	0.244	0.069	0.301	0.075	99.8	1.640	0.395	26.555	24.533	7.5	1.355	0.503	45.092	34.987	3.2	1.431	0.618	46.972	45.065	2.2	28.2
BUFFER [2]	0.259	0.072	0.262	0.079	99.8	0.437	<u>0.131</u>	0.475	0.345	<u>98.6</u>	0.719	0.230	2.290	1.910	<u>93.5</u>	1.050	0.364	14.221	15.811	<u>61.2</u>	<u>88.3</u>
PARE [38]	0.239	0.054	0.242	0.061	99.8	1.284	0.401	19.192	27.340	1.8	–	–	23.682	37.837	0.0	–	–	29.139	47.570	0.0	25.4
CoFiNet w/o C	<u>0.366</u>	<u>0.085</u>	<u>0.379</u>	<u>0.109</u>	99.8	0.813	<u>0.182</u>	<u>2.305</u>	<u>1.504</u>	<u>92.5</u>	<u>1.734</u>	<u>0.490</u>	<u>14.172</u>	<u>18.061</u>	<u>35.1</u>	<u>1.970</u>	<u>0.785</u>	<u>27.077</u>	<u>36.130</u>	<u>7.9</u>	<u>58.8</u>
GeoTrans w/o C	<u>0.238</u>	0.066	0.295	0.073	99.8	0.426	0.146	0.501	0.225	<u>98.6</u>	<u>0.699</u>	<u>0.285</u>	4.808	1.889	<u>93.5</u>	0.949	0.476	32.318	14.096	59.0	87.7
PARE w/o C	<u>0.289</u>	<u>0.071</u>	<u>0.292</u>	<u>0.078</u>	99.8	0.924	0.288	9.548	4.627	73.0	1.330	<u>0.574</u>	38.783	23.824	15.7	3.660	1.456	47.526	39.225	0.7	47.3
UGP(Ours)	<u>0.245</u>	<u>0.071</u>	<u>0.298</u>	<u>0.078</u>	99.8	<u>0.393</u>	<u>0.147</u>	0.449	0.221	99.3	0.677	<u>0.290</u>	2.127	0.805	96.8	<u>0.975</u>	<u>0.494</u>	13.095	6.168	82.0	94.5

Model	Train on nuScenes@10m					nuScenes@20m					nuScenes@30m					nuScenes@40m					mRR
	RRE	RTE	RRE*	RTE*	RR	RRE	RTE	RRE*	RTE*	RR	RRE	RTE	RRE*	RTE*	RR	RRE	RTE	RRE*	RTE*	RR	
FCGF [8]	0.338	0.176	0.396	0.374	97.4	<u>0.511</u>	0.343	2.524	3.105	84.4	1.015	0.492	6.801	12.178	53.5	1.560	0.519	12.496	28.355	19.7	<u>63.8</u>
Predator [16]	0.365	<u>0.178</u>	0.365	0.178	100	1.640	0.312	22.617	10.038	15.8	1.855	0.279	25.102	20.76	5.3	1.809	<u>0.175</u>	31.424	29.966	5.1	31.6
CoFiNet [39]	0.461	0.195	0.625	0.416	97.0	1.370	0.482	18.662	7.398	58.0	1.810	0.556	33.388	23.109	12.7	1.923	0.365	32.966	33.459	6.5	43.6
GeoTrans [28]	0.259	<u>0.178</u>	0.259	0.178	100	0.733	0.412	9.099	5.059	57.1	<u>0.734</u>	0.382	22.755	19.452	9.6	<u>0.571</u>	0.294	29.104	29.317	7.2	43.5
BUFFER [2]	0.340	<u>0.178</u>	0.390	0.394	97.5	0.528	0.347	<u>0.866</u>	<u>2.917</u>	<u>84.7</u>	0.918	0.523	9.901	14.183	46.6	1.073	0.567	25.865	30.811	15.2	61.0
PARE [38]	0.449	0.190	0.475	0.202	<u>99.7</u>	0.906	0.445	6.834	9.638	9.2	0.674	<u>0.365</u>	10.530	19.084	5.3	0.346	0.163	13.746	<u>28.349</u>	4.6	29.7
UGP(Ours)	<u>0.270</u>	0.179	<u>0.270</u>	<u>0.179</u>	100	0.467	<u>0.338</u>	0.646	0.415	99.4	0.780	0.460	1.284	1.456	93.9	1.142	0.636	10.532	8.641	72.3	91.4

Table 1. **Cross-distance generalization experiments.** For both the KITTI and nuScenes datasets, we train at 10m and then test at 10m and farther distances at 20m, 30m, and 40m. RRE and RTE denote the error for successfully matched point cloud pairs, while RRE* and RTE* reflect the error for all point cloud pairs, providing a more comprehensive evaluation. The final column shows the mean Registration Recall.

points. The mask $M_{i,j}^{(L=k)}$ is computed by dividing the maximum distance between superpoint \hat{p}_i and all other superpoints \hat{p}_j in the \hat{P} into S segments. For a given layer $L = k$, the mask is defined as:

$$M_{i,j}^{(L=k)} = \begin{cases} 1, & \text{if } d_{i,j} \leq \frac{k \cdot d_{i,\max}}{S}, k = 1, 2, \dots, S \\ 0, & \text{otherwise} \end{cases}, \quad (5)$$

where $d_{i,\max} = \max_{i,j \in \hat{P}} d_{i,j}$, k represents the segment index, with $k = 1$ corresponding to the smallest distance range and $k = S$ corresponding to the largest. This enables the model to gradually expand the receptive field, focus on more refined local space in the early stage, reduce distant noise, and then learn multi-scale spatial feature expressions. After performing S iterations of attention, the mixed superpoint features $\mathbf{H}^{\hat{P}}$ and $\mathbf{H}^{\hat{Q}}$ are obtained.

Superpoint Matching. To obtain the superpoint correspondences, we follow [28]. First, the features $\mathbf{H}^{\hat{P}}$ and $\mathbf{H}^{\hat{Q}}$ obtained in the coarse stage are normalized to the unit sphere to yield the features $\bar{\mathbf{H}}^{\hat{P}}$ and $\bar{\mathbf{H}}^{\hat{Q}}$. Next, we compute a Gaussian correlation matrix $\hat{\mathbf{S}}$ with $\hat{s}_{i,j} = \exp\left(-\left\|\bar{\mathbf{h}}_i^{\hat{P}} - \bar{\mathbf{h}}_j^{\hat{Q}}\right\|_2^2\right)$. Following this, we perform dual normalization on $\hat{\mathbf{S}}$ to obtain $\bar{\mathbf{S}}$. Finally, based on the normalized results, the top- k point pairs with the highest correlation scores are selected as superpoint correspondences $\hat{C} = \{(\hat{p}_i, \hat{q}_j) \mid (\hat{p}_i, \hat{q}_j) \in \text{topk}(\bar{\mathbf{S}})\}$.

5. Experiments

5.1. Experimental Settings

Datasets. We evaluated our method on two outdoor LiDAR datasets: KITTI (64-line LiDAR) [12] and nuScenes (32-line LiDAR) [4]. Following previous works [8, 16, 39], sequences 0-5 are used for training, 6-7 for validation, and 8-10 for testing, with pairs created from scans at least 10m apart. To evaluate cross-distance and cross-dataset generalization, we expanded the test set to include pairs separated by 20m, 30m, and 40m. The goal is to train on the KITTI@10m dataset and test generalization on KITTI@20m, KITTI@30m and KITTI@40m. For nuScenes, we follow the common protocol [4], splitting it into training, validation, and testing subsets. Using the same approach, we train and validate on nuScenes@10m and test on nuScenes@20m, nuScenes@30m, and nuScenes@40m. To verify cross-dataset generalization, we trained on nuScenes@10m and tested on KITTI@10m, KITTI@20m, KITTI@30m, and KITTI@40m. Additional experiments are in Appendix Sec. 9.

Metrics. We follow the previous work [6, 16, 28] and use five evaluation metrics: Patch Inlier Ratio (PIR), Inlier Ratio (IR), Relative Rotation Error (RRE), Relative Translation Error (RTE), Registration Recall (RR), and mean Registration Recall (mRR). RR in all experiments is based on the criteria $RRE < 5^\circ$ and $RTE < 2m$. The definitions of the metrics can be found in Appendix Sec. 8.

5.2. Generalization Experiment

Cross-Distance Generalization. We compare the proposed UGP with other state-of-the-art methods in KITTI and

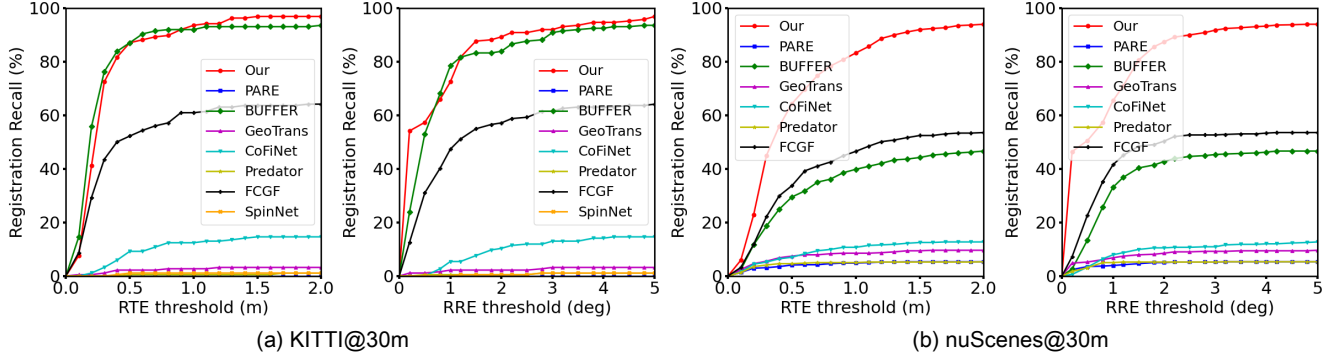


Figure 5. Cross-distance registration recall results of different RRE and RTE thresholds on the KITTI@30m and nuScenes@30m.

Model	KITTI@10m					KITTI@20m					KITTI@30m					KITTI@40m					
	RRE	RTE	RRE*	RTE*	RR	RRE	RTE	RRE*	RTE*	RR	RRE	RTE	RRE*	RTE*	RR	RRE	RTE	RRE*	RTE*	RR	mRR
FCGF [8]	0.196	0.060	1.455	0.248	<u>98.0</u>	0.345	0.105	5.739	1.458	92.2	0.701	0.219	10.413	5.949	79.5	1.398	0.350	17.755	20.333	46.0	78.9
Predator [16]	0.415	0.093	1.086	0.254	97.8	1.267	0.249	9.003	7.430	59.4	1.881	0.279	19.460	28.709	0.5	-	-	26.632	38.956	0.0	39.4
CoFiNet [39]	0.345	0.084	0.345	0.090	99.8	0.939	0.201	3.355	1.541	90.0	1.843	0.610	13.620	17.622	31.9	2.181	1.183	26.385	36.950	4.3	56.5
GeoTrans [28]	0.550	0.130	8.157	6.938	51.4	0.894	0.315	16.391	8.515	45.2	1.593	0.557	44.138	21.729	13.5	1.974	0.847	43.806	32.264	10.8	30.2
BUFFER [2]	<u>0.261</u>	<u>0.065</u>	0.264	0.072	99.8	0.508	<u>0.135</u>	0.539	<u>0.349</u>	<u>98.6</u>	0.780	<u>0.265</u>	4.873	<u>3.542</u>	<u>87.0</u>	<u>1.058</u>	<u>0.396</u>	21.435	<u>17.723</u>	<u>53.2</u>	<u>84.7</u>
PARE [38]	0.557	0.160	16.274	4.878	57.3	1.739	0.700	45.434	18.671	2.1	-	-	54.498	29.199	0.0	-	-	65.780	39.359	0.0	14.9
GCL [19]	<u>0.265</u>	<u>0.078</u>	<u>0.680</u>	<u>0.129</u>	<u>99.5</u>	<u>0.448</u>	<u>0.116</u>	<u>5.169</u>	<u>1.311</u>	<u>93.2</u>	<u>0.742</u>	<u>0.173</u>	<u>9.694</u>	<u>4.626</u>	<u>83.8</u>	<u>1.262</u>	<u>0.309</u>	<u>19.348</u>	<u>13.943</u>	<u>63.3</u>	<u>85.0</u>
UGP (Ours)	<u>0.282</u>	<u>0.078</u>	<u>0.287</u>	<u>0.085</u>	99.8	<u>0.497</u>	<u>0.166</u>	<u>1.098</u>	0.309	98.9	<u>0.769</u>	<u>0.333</u>	<u>5.287</u>	1.867	90.8	0.975	0.523	<u>18.260</u>	8.791	74.1	90.9

Table 2. Cross-dataset generalization experiments. We train on the nuScenes@10m dataset and then test on the KITTI@10m, KITTI@20m, KITTI@30m and KITTI@40m. ‘†’ denotes that the method was trained using data within the range of [5m, 60m].

nuScenes. Experimental results are shown in Tab. 1. Our method surpasses all the above approaches in terms of RR on both the KITTI and nuScenes datasets, particularly outperforming BUFFER. Compared to BUFFER, our method improves KITTI mRR by 6.2% and KITTI@40m RR by 20.8%. Furthermore, on the much sparser nuScenes dataset, our method significantly outperforms all other methods. Our method achieves SOTA at nuScenes@10m and then at nuScenes@20m improves by 42.3% compared to GeoTrans, 14.7% compared to BUFFER and 15% compared to FCGF. At 30m our method still maintains 93.9%, and outperforms BUFFER by 47.3%. On the challenging 40m our method improves 57.1% compared to BUFFER.

We further analyze the influence of point cloud pair distance changes on different methods. For coarse-to-fine methods (CoFiNet, GeoTransformer and PARE) performance drops significantly as point cloud pair distance changes. Even when generalizing to the relatively simpler 20m data subset, GeoTransformer’s RR drops to 7.5%, while PARE’s RR drops to 1.8%, and their performance continues to degrade as the distance increases. In contrast, for the point-wise or patch-wise methods (FCGF and BUFFER), which avoid inter-frame information exchange in their network design, retain their generalization capability. When the cross attention is eliminated (CoFiNet.w/o C, GeoTrans.w/o C and PARE.w/o C in Tab. 1), the generalization capability is unlocked. This further validates that the elimination of the cross-attention module plays a key role in

enhancing the generalization of LiDAR scenes.

To evaluate the overall performance of our method, we also included average error metrics RRE* and RTE* for all test point pairs. Our method achieves the highest accuracy in terms of average RRE and RTE across all test point pairs for the 20m, 30m, and 40m distance generalization experiments. We display the cross-distance generalization registration recall with different RRE and RTE thresholds on two datasets in Fig. 5. According to this result, while the performance of BUFFER in KITTI@30m is higher than our method at some thresholds, we show a very large improvement at all thresholds in the larger nuScenes dataset test.

Model	nuScenes@10m				
	RRE(°)	RTE(m)	RRE*(°)	RTE*(m)	RR(%)
FCGF [8]	<u>0.390</u>	<u>0.195</u>	0.889	0.711	93.3
SpinNet [1]	1.941	0.390	10.714	7.562	7.1
Predator [16]	1.034	0.265	5.146	1.708	80.2
CoFiNet [39]	0.713	0.231	0.959	1.122	88.5
GeoTrans [28]	0.920	0.288	12.313	6.500	44.3
Buffer [2]	0.367	0.183	0.435	<u>0.626</u>	<u>94.3</u>
PARE [38]	1.371	0.402	7.901	6.489	52.5
UGP(Ours)	0.422	0.199	<u>0.478</u>	0.322	98.4

Table 3. The results of the cross-dataset generalization experiments from KITTI@10m to nuScenes@10m.

Cross-Datasets Generalization. To evaluate the cross-dataset generalization capability of the proposed UGP, we

				KITTI@30m						
No.	EC	PSA	BF	PIR	IR	RRE	RTE	RRE*	RTE*	RR
a	-	-	-	1.3	1.5	1.712	0.531	37.897	33.874	6.5
b	✓	-	-	49.7	39.4	<u>0.657</u>	0.280	2.155	0.899	95.1
c	✓	✓	-	54.5	38.5	0.658	0.306	<u>2.090</u>	0.541	<u>96.2</u>
d	✓	-	✓	56.1	41.5	0.619	0.294	2.032	<u>0.681</u>	95.7
e	✓	✓	✓	57.6	<u>40.6</u>	0.677	<u>0.290</u>	2.127	0.805	96.8

				KITTI@40m						
No.	EC	PSA	BF	PIR	IR	RRE	RTE	RRE*	RTE*	RR
a	-	-	-	0.8	0.7	2.101	0.967	54.430	46.728	2.2
b	✓	-	-	24.2	18.2	0.950	0.486	21.539	10.401	66.2
c	✓	✓	-	28.3	18.5	<u>0.909</u>	<u>0.470</u>	17.692	9.091	71.2
d	✓	-	✓	<u>29.9</u>	20.3	0.907	0.461	<u>14.650</u>	<u>8.967</u>	<u>74.8</u>
e	✓	✓	✓	32.5	<u>19.9</u>	0.975	0.494	13.095	6.168	82.0

Table 4. **Ablation experiment** analysis of UGP on KITTI. Eliminating the cross-attention module (EC), progressive self-attention module (PSA), BEV fusion (BF) are ablated.

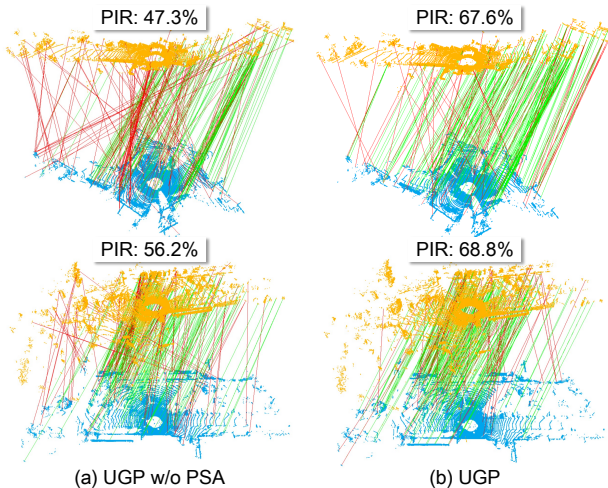


Figure 6. Registration results of the models with (a) vanilla self-attention and (b) progressive self-attention.

conducted the following experiments: 1) from nuScenes to KITTI@ (10m, 20m, 30m and 40m), 2) from KITTI to nuScenes. As shown in Tab. 2, the proposed UGP method, at KITTI@10m, achieved 99.8% registration recall. Also on KITTI@20m, KITTI@30m and KITTI@40m, the best results 98.9% (+0.3%), 90.8% (+3.8%) and 74.1% (+20.9%) were achieved compared to BUFFER. It can be found that our method has a significant advantage at longer distances. Finally, we compared the GCL [19] method using the pre-training weights of GCL in nuScenes. It can be found that our method also has a significant improvement in cross-dataset generalization compared to GCL, even though GCL utilizes [5m, 60m] point cloud frame during training. As shown in Tab. 3, our method achieves the best results despite the differences in sensor beams (KITTI: 64-line, nuScenes: 32-line). Compared to the sub-optimal BUFFER, the RR of our method improves by 4.1%.

5.3. Ablation Study

Ablation of Backbone. First, we performed an ablation study on the core components of the method to demonstrate the effectiveness of each part, as shown in Tab. 4. By comparing rows *a-b* in Tab. 4, we can see that EC significantly improves the network’s generalization capability. By comparing rows *b-c*, we observe that PSA improves PIR by 4.8% and increases RR on KITTI@30m by 1.1% and by 5% at longer distances (40m) compared to the vanilla self-attention module. We further visualize the matching results of the ablation PSA, as shown in Fig. 6. It can be seen that the number of long-distance false matches is reduced significantly in the figure, proving that our PSA can effectively solve the feature ambiguity problem in vanilla self-attention. By comparing rows *b-d* and *c-e*, it can be observed that BEV provides semantic information about scene elements, reducing scene ambiguity. As a result, the framework’s PIR and RR both improve. Column *e* in the table represents our complete proposed method, which achieves the best performance in the key metric of RR.

Estimators	mRR	KITTI@10m	KITTI@20m	KITTI@30m	KITTI@40m
UGP+RANSAC50K	92.4	99.8	99.3	95.1	75.5
UGP+MAC	94.9	99.8	99.3	<u>96.2</u>	84.2
UGP+LGR	<u>94.5</u>	99.8	99.3	96.8	<u>82.0</u>

Table 5. **Comparison of cross-distance generalization performance** for different estimators on KITTI.

Ablation of Estimator. We evaluated the impact of different estimators on the registration results, as shown in Tab. 5. The mRR of our method with RANSAC [11] is 92.4%, with MAC [42] is 94.9%, and with LGR [28] is 94.5%.

6. Conclusion

In this paper, we revealed that inconsistent geometric representations in LiDAR scenarios cause the cross-attention module to limit network generalization capability. Based on this insight, we proposed UGP, a pruned framework designed to enhance generalization power for LiDAR point cloud registration. UGP eliminated cross-attention, introduced a progressive self-attention module and a BEV feature extraction module, enabling the network to prioritize local spatial associations and captured semantic information of scene elements. This reduced ambiguity in point clouds and boosted generalization performance. Extensive experiments showed that our method effectively addresses challenges across varying data distributions, including cross-distance and cross-dataset scenarios.

Acknowledgments. This work is supported in part by the National Natural Science Foundation of China (No.U23B2013 and 62372377).

References

- [1] Sheng Ao, Qingyong Hu, Bo Yang, Andrew Markham, and Yulan Guo. Spinnet: Learning a general surface descriptor for 3d point cloud registration. In *Proceedings of the IEEE/CVF Conference on Computer Vision and Pattern Recognition*, pages 11753–11762, 2021. 1, 2, 6, 7
- [2] Sheng Ao, Qingyong Hu, Hanyun Wang, Kai Xu, and Yulan Guo. Buffer: Balancing accuracy, efficiency, and generalizability in point cloud registration. In *Proceedings of the IEEE/CVF Conference on Computer Vision and Pattern Recognition*, pages 1255–1264, 2023. 2, 6, 7, 3, 5
- [3] Xuyang Bai, Zixin Luo, Lei Zhou, Hongbo Fu, Long Quan, and Chiew-Lan Tai. D3feat: Joint learning of dense detection and description of 3d local features. In *Proceedings of the IEEE/CVF Conference on Computer Vision and Pattern Recognition*, pages 6359–6367, 2020. 1, 2
- [4] Holger Caesar, Varun Bankiti, Alex H Lang, Sourabh Vora, Venice Erin Liong, Qiang Xu, Anush Krishnan, Yu Pan, Giancarlo Baldan, and Oscar Beijbom. nuscenes: A multi-modal dataset for autonomous driving. In *Proceedings of the IEEE/CVF Conference on Computer Vision and Pattern Recognition*, pages 11621–11631, 2020. 1, 6
- [5] Anh-Quan Cao, Gilles Puy, Alexandre Boulch, and Renaud Marlet. Pcam: Product of cross-attention matrices for rigid registration of point clouds. In *Proceedings of the IEEE/CVF International Conference on Computer Vision*, pages 13229–13238, 2021. 1
- [6] Hong Chen, Pei Yan, Sihe Xiang, and Yihua Tan. Dynamic cues-assisted transformer for robust point cloud registration. In *Proceedings of the IEEE/CVF Conference on Computer Vision and Pattern Recognition*, pages 21698–21707, 2024. 2, 5, 6
- [7] Christopher Choy, JunYoung Gwak, and Silvio Savarese. 4d spatio-temporal convnets: Minkowski convolutional neural networks. In *Proceedings of the IEEE/CVF Conference on Computer Vision and Pattern Recognition*, pages 3075–3084, 2019. 2
- [8] Christopher Choy, Jaesik Park, and Vladlen Koltun. Fully convolutional geometric features. In *Proceedings of the IEEE/CVF International Conference on Computer Vision*, pages 8958–8966, 2019. 2, 6, 7, 3
- [9] Haowen Deng, Tolga Birdal, and Slobodan Ilic. Ppfnet: Global context aware local features for robust 3d point matching. In *Proceedings of the IEEE Conference on Computer Vision and Pattern Recognition*, pages 195–205, 2018. 1, 2
- [10] Mohamed El Banani and Justin Johnson. Bootstrap your own correspondences. In *Proceedings of the IEEE/CVF International Conference on Computer Vision*, pages 6433–6442, 2021. 3
- [11] Martin A Fischler and Robert C Bolles. Random sample consensus: a paradigm for model fitting with applications to image analysis and automated cartography. *Communications of the ACM*, 24(6):381–395, 1981. 8
- [12] Andreas Geiger, Philip Lenz, and Raquel Urtasun. Are we ready for autonomous driving? the kitti vision benchmark suite. In *Proceedings of the IEEE/CVF Conference on Computer Vision and Pattern Recognition*, pages 3354–3361. IEEE, 2012. 6, 5
- [13] Zan Gojcic, Caifa Zhou, Jan D Wegner, and Andreas Wieser. The perfect match: 3d point cloud matching with smoothed densities. In *Proceedings of the IEEE/CVF Conference on Computer Vision and Pattern Recognition*, pages 5545–5554, 2019. 1, 2
- [14] Yulan Guo, Mohammed Bennamoun, Ferdous Sohel, Min Lu, and Jianwei Wan. 3d object recognition in cluttered scenes with local surface features: A survey. *IEEE Transactions on Pattern Analysis and Machine Intelligence*, 36(11): 2270–2287, 2014. 1
- [15] Kaiming He, Xiangyu Zhang, Shaoqing Ren, and Jian Sun. Deep residual learning for image recognition. In *Proceedings of the IEEE Conference on Computer Vision and Pattern Recognition*, pages 770–778, 2016. 5, 1
- [16] Shengyu Huang, Zan Gojcic, Mikhail Usvyatsov, Andreas Wieser, and Konrad Schindler. Predator: Registration of 3d point clouds with low overlap. In *Proceedings of the IEEE/CVF Conference on Computer Vision and Pattern Recognition*, pages 4267–4276, 2021. 1, 6, 7, 2
- [17] Diederik P Kingma. Adam: A method for stochastic optimization. *arXiv preprint arXiv:1412.6980*, 2014. 1
- [18] Quan Liu, Yunsong Zhou, Hongzi Zhu, Shan Chang, and Minyi Guo. Apr: online distant point cloud registration through aggregated point cloud reconstruction. In *Proceedings of the International Joint Conference on Artificial Intelligence*, 2023. 2
- [19] Quan Liu, Hongzi Zhu, Yunsong Zhou, Hongyang Li, Shan Chang, and Minyi Guo. Density-invariant features for distant point cloud registration. In *Proceedings of the IEEE/CVF International Conference on Computer Vision*, pages 18215–18225, 2023. 7, 8
- [20] Quan Liu, Hongzi Zhu, Zhenxi Wang, Yunsong Zhou, Shan Chang, and Minyi Guo. Extend your own correspondences: Unsupervised distant point cloud registration by progressive distance extension. In *Proceedings of the IEEE/CVF Conference on Computer Vision and Pattern Recognition*, pages 20816–20826, 2024. 2
- [21] Zhe Liu, Shunbo Zhou, Chuanzhe Suo, Peng Yin, Wen Chen, Hesheng Wang, Haoang Li, and Yun-Hui Liu. Lpd-net: 3d point cloud learning for large-scale place recognition and environment analysis. In *Proceedings of the IEEE/CVF International Conference on Computer Vision*, pages 2831–2840, 2019. 4
- [22] Lun Luo, Shuhang Zheng, Yixuan Li, Yongzhi Fan, Beinan Yu, Si-Yuan Cao, Junwei Li, and Hui-Liang Shen. Bevplace: Learning lidar-based place recognition using bird’s eye view images. In *Proceedings of the IEEE/CVF International Conference on Computer Vision*, pages 8700–8709, 2023. 3
- [23] Juncheng Mu, Lin Bie, Shaoyi Du, and Yue Gao. Colorpcr: Color point cloud registration with multi-stage geometric-color fusion. In *Proceedings of the IEEE/CVF Conference on Computer Vision and Pattern Recognition*, pages 21061–21070, 2024. 2
- [24] Raul Mur-Artal and Juan D Tardós. Orb-slam2: An open-source slam system for monocular, stereo, and rgb-d cam-

- eras. *IEEE Transactions on Robotics*, 33(5):1255–1262, 2017. 1
- [25] Raul Mur-Artal, Jose Maria Martinez Montiel, and Juan D Tardos. Orb-slam: a versatile and accurate monocular slam system. *IEEE Transactions on Robotics*, 31(5):1147–1163, 2015. 1
- [26] Adam Paszke, Sam Gross, Francisco Massa, Adam Lerer, James Bradbury, Gregory Chanan, Trevor Killeen, Zeming Lin, Natalia Gimelshein, Luca Antiga, et al. Pytorch: An imperative style, high-performance deep learning library. *Advances in neural information processing systems*, 32, 2019. 1
- [27] Fabio Poiesi and Davide Boscaini. Learning general and distinctive 3d local deep descriptors for point cloud registration. *IEEE Transactions on Pattern Analysis and Machine Intelligence*, 45(3):3979–3985, 2022. 1, 2
- [28] Zheng Qin, Hao Yu, Changjian Wang, Yulan Guo, Yuxing Peng, and Kai Xu. Geometric transformer for fast and robust point cloud registration. In *Proceedings of the IEEE/CVF Conference on Computer Vision and Pattern Recognition*, pages 11143–11152, 2022. 1, 2, 3, 4, 5, 6, 7, 8
- [29] Tixiao Shan, Brendan Englot, Drew Meyers, Wei Wang, Carlo Ratti, and Daniela Rus. Lio-sam: Tightly-coupled lidar inertial odometry via smoothing and mapping. In *2020 IEEE/RSJ international conference on intelligent robots and systems (IROS)*, pages 5135–5142. IEEE, 2020. 1
- [30] Richard Sinkhorn and Paul Knopp. Concerning nonnegative matrices and doubly stochastic matrices. *Pacific Journal of Mathematics*, 21(2):343–348, 1967. 1
- [31] Pei Sun, Henrik Kretzschmar, Xerxes Dotiwalla, Aurelien Chouard, Vijaysai Patnaik, Paul Tsui, James Guo, Yin Zhou, Yuning Chai, Benjamin Caine, et al. Scalability in perception for autonomous driving: Waymo open dataset. In *Proceedings of the IEEE/CVF Conference on Computer Vision and Pattern Recognition*, pages 2446–2454, 2020. 2
- [32] Hugues Thomas, Charles R Qi, Jean-Emmanuel Deschaud, Beatriz Marcotegui, François Goulette, and Leonidas J Guibas. Kpconv: Flexible and deformable convolution for point clouds. In *Proceedings of the IEEE/CVF International Conference on Computer Vision*, pages 6411–6420, 2019. 2, 4, 5, 1
- [33] A Vaswani. Attention is all you need. *Advances in Neural Information Processing Systems*, 2017. 2, 4
- [34] Kezheng Xiong, Maoji Zheng, Qingshan Xu, Chenglu Wen, Siqi Shen, and Cheng Wang. Speal: Skeletal prior embedded attention learning for cross-source point cloud registration. In *Proceedings of the AAAI Conference on Artificial Intelligence*, pages 6279–6287, 2024. 2
- [35] Jianyun Xu, Ruixiang Zhang, Jian Dou, Yushi Zhu, Jie Sun, and Shiliang Pu. Rpvnet: A deep and efficient range-point-voxel fusion network for lidar point cloud segmentation. In *Proceedings of the IEEE/CVF International Conference on Computer Vision*, pages 16024–16033, 2021. 3, 4
- [36] Zongyi Xu, Xinqi Jiang, Xinyu Gao, Rui Gao, Changjun Gu, Qianni Zhang, Weisheng Li, and Xinbo Gao. Igreg: Image-geometry-assisted point cloud registration via selective correlation fusion. *IEEE Transactions on Multimedia*, 2024. 3
- [37] Bin Yang, Wenjie Luo, and Raquel Urtasun. Pixor: Real-time 3d object detection from point clouds. In *Proceedings of the IEEE/CVF Conference on Computer Vision and Pattern Recognition*, 2018. 3
- [38] Runzhao Yao, Shaoyi Du, Wenting Cui, Canhui Tang, and Chengwu Yang. Pare-net: Position-aware rotation-equivariant networks for robust point cloud registration. *arXiv preprint arXiv:2407.10142*, 2024. 1, 2, 3, 5, 6, 7
- [39] Hao Yu, Fu Li, Mahdi Saleh, Benjamin Busam, and Slobodan Ilic. Cofinet: Reliable coarse-to-fine correspondences for robust pointcloud registration. *Advances in Neural Information Processing Systems*, 34:23872–23884, 2021. 1, 2, 3, 5, 6, 7
- [40] Hao Yu, Zheng Qin, Ji Hou, Mahdi Saleh, Dongsheng Li, Benjamin Busam, and Slobodan Ilic. Rotation-invariant transformer for point cloud matching. In *Proceedings of the IEEE/CVF Conference on Computer Vision and Pattern Recognition*, pages 5384–5393, 2023. 1
- [41] Junle Yu, Luwei Ren, Yu Zhang, Wenhui Zhou, Lili Lin, and Guojun Dai. Peal: Prior-embedded explicit attention learning for low-overlap point cloud registration. In *Proceedings of the IEEE/CVF Conference on Computer Vision and Pattern Recognition*, pages 17702–17711, 2023. 2, 3, 5
- [42] Xiyu Zhang, Jiaqi Yang, Shikun Zhang, and Yanning Zhang. 3d registration with maximal cliques. In *Proceedings of the IEEE/CVF Conference on Computer Vision and Pattern Recognition*, pages 17745–17754, 2023. 8
- [43] Yu Zhang, Junle Yu, Xiaolin Huang, Wenhui Zhou, and Ji Hou. Pcr-cg: Point cloud registration via deep explicit color and geometry. In *Proceedings of the European Conference on Computer Vision*, pages 443–459. Springer, 2022. 3

Unlocking Generalization Power in LiDAR Point Cloud Registration

Supplementary Material

7. Method Details

Backbone. Our Point-Encoder and Point-Decoder follow the KPConv-FPN [32] structure to perform point-level feature extraction. Before inputting the points into the Point-Encoder, we voxel downsample the KITTI point cloud with a voxel size of 0.3m and the nuScenes point cloud with a voxel size of 0.2m. The Point-Encoder and Point-Decoder follow GeoTrans [28], with 5 and 3 layers, respectively. For the BEV-Encoder, we adopt a ResNet-like [15] structure with 3 layers.

BEV Patch and Superpoint Indexing. Given the superpoints, their 3D coordinates are projected onto the resolution $(H \times W)$ of the original BEV image. By accounting for the number of 2D max pooling operations β , we determine the index of each superpoint relative to the downsampled BEV patch. This correspondence establishes a one-to-one mapping between the features of the superpoints and BEV patches. Let (u_i, v_i) represent the 2D coordinates of a superpoint in the BEV image. The corresponding index in the downsampled BEV feature map is calculated as:

$$u_i = \left\lfloor \frac{u_i}{2^\beta} \right\rfloor, \quad v_i = \left\lfloor \frac{v_i}{2^\beta} \right\rfloor. \quad (6)$$

Here, (u'_i, v'_i) represents the index of the patch feature in the downsampled BEV image.

Point Matching. After obtaining the superpoint correspondences $\hat{\mathcal{C}}$, we follow a point-to-node assignment strategy [28] to uniquely assign dense points $\tilde{\mathbf{P}}$ and $\tilde{\mathbf{Q}}$ to their nearest superpoints, resulting in groups \mathcal{G}^P and \mathcal{G}^Q . Then, based on the superpoint correspondences $\hat{\mathcal{C}}$, we perform local dense matching. Unlike previous work, we input the attention features $\tilde{\mathbf{H}}^{\tilde{\mathbf{P}}}$ and $\tilde{\mathbf{H}}^{\tilde{\mathbf{Q}}}$ into the Point-Decoder to obtain dense point features $\mathbf{F}_{\tilde{\mathbf{P}}} \in \mathbb{R}^{\tilde{n} \times \tilde{d}}$ and $\mathbf{F}_{\tilde{\mathbf{Q}}} \in \mathbb{R}^{\tilde{m} \times \tilde{d}}$. For a given superpoint correspondence $\hat{\mathcal{C}}_i$ and its corresponding local dense points \mathcal{G}_i^P and \mathcal{G}_i^Q , we compute the cost matrix $\tilde{\mathbf{C}}$, where $\tilde{\mathbf{C}}_i = \mathbf{F}_{\tilde{\mathbf{P}}}^i \left(\mathbf{F}_{\tilde{\mathbf{Q}}}^i \right)^T / \sqrt{\tilde{d}}$. Then, we use the Sinkhorn algorithm [30] to recompute the similarity matrix, resulting in $\tilde{\mathbf{C}}$. Based on $\tilde{\mathbf{C}}$, we apply mutual top- k to select the dense point correspondences. Finally, we gather all the dense point correspondences $\tilde{\mathcal{C}}_i$ for each coarse match in $\hat{\mathcal{C}}$, forming the final dense point correspondences $\mathcal{C} = \bigcup_{i=1}^{|\hat{\mathcal{C}}|} \tilde{\mathcal{C}}_i$.

Loss Function. Our framework’s loss function consists of two components, $\mathcal{L} = \mathcal{L}_c + \mathcal{L}_f$, where L_c and L_f represent the same superpoint matching loss and point matching loss as [28].

Implementation Details. We conduct our experiments using PyTorch [26] on an Intel (R) Xeon (R) Gold 5118 CPU

and an NVIDIA RTX 3090 GPU. The Adam optimizer [17] is used to train our model, with an initial learning rate of 1e-4 and a weight decay of 1e-6.

8. Evaluation Metrics

We follow previous work [28] and report Patch Inlier Ratio (PIR), Inlier Ratio (IR), Relative Rotation Error (RRE), Relative Translation Error (RTE) and Registration Recall (RR). **Patch Inlier Ratio (PIR)** represents the proportion of superpoint (patch) matches that correctly overlap when aligned using the ground-truth transformation $\mathbf{T}_{\mathbf{P} \rightarrow \mathbf{Q}}$. This metric indicates the reliability and accuracy of the proposed superpoint (patch) correspondences:

$$\text{PIR} = \frac{1}{|\hat{\mathcal{C}}|} \sum_{(\tilde{p}_i, \tilde{q}_j) \in \hat{\mathcal{C}}} \mathbb{1}(\exists \tilde{\mathbf{p}} \in \mathcal{G}_i^P, \tilde{\mathbf{q}} \in \mathcal{G}_j^Q \text{ s.t. } \|\mathbf{T}_{\mathbf{P} \rightarrow \mathbf{Q}}(\tilde{\mathbf{p}}) - \tilde{\mathbf{q}}\|_2 < \tau), \quad (7)$$

where $\tau = 0.6\text{m}$ and $\mathbb{1}$ is the indicator function.

Inlier Ratio (IR) represents the proportion of inlier matches among all candidate point correspondences. A match qualifies as an inlier if the distance between the two points transformed by the ground-truth transformation $\mathbf{T}_{\mathbf{P} \rightarrow \mathbf{Q}}$ is less than a threshold $\tau_1 = 1.0\text{m}$:

$$\text{IR} = \frac{1}{|\mathcal{C}|} \sum_{(\tilde{p}_i, \tilde{q}_j) \in \mathcal{C}} \mathbb{1}(\|\mathbf{T}_{\mathbf{P} \rightarrow \mathbf{Q}}(\tilde{\mathbf{p}}_i) - \tilde{\mathbf{q}}_j\|_2 < \tau_1). \quad (8)$$

Relative Rotation Error (RRE) represents the geodesic distance measured in degrees between the estimated \mathbf{R}_{est} and ground-truth \mathbf{R}_{gt} rotation matrices. It quantifies the discrepancy between the predicted and actual rotation matrices:

$$\text{RRE} = \arccos \left(\frac{\text{trace}(\mathbf{R}_{est}^T \cdot \mathbf{R}_{gt}) - 1}{2} \right). \quad (9)$$

Relative Translation Error (RTE) represents the Euclidean distance between the estimated \mathbf{t}_{est} and ground-truth \mathbf{t}_{gt} translation vectors. This metric assesses the difference between the estimated and ground-truth translation vectors:

$$\text{RTE} = \|\mathbf{t}_{est} - \mathbf{t}_{gt}\|_2. \quad (10)$$

Registration Recall (RR) for all outdoor datasets is defined as the proportion of point cloud pairs where both RRE and RTE fall below specified thresholds ($\text{RRE} < 5^\circ$ and $\text{RTE} < 2\text{m}$):

$$\text{RR} = \frac{1}{M} \sum_{i=1}^M \mathbb{1}(\text{RRE}_i < 5^\circ \wedge \text{RTE}_i < 2\text{m}), \quad (11)$$

Model	KITTI@10m					KITTI@20m					KITTI@30m					Train on KITTI@40m					mRR
	RRE	RTE	RRE*	RTE*	RR	RRE	RTE	RRE*	RTE*	RR	RRE	RTE	RRE*	RTE*	RR	RRE	RTE	RRE*	RTE*	RR	
FCGF [8]	1.180	0.285	<u>6.713</u>	3.304	65.6	1.846	0.532	15.044	18.343	5.0	-	-	21.267	29.356	0.0	2.089	<u>0.524</u>	23.732	39.583	0.7	17.8
Predator [16]	1.560	1.073	7.622	9.567	0.4	-	-	<u>14.587</u>	19.495	0.0	1.873	0.607	18.341	29.323	0.5	2.037	1.165	22.941	38.708	0.7	0.4
CoFiNet [39]	1.325	0.280	7.400	3.420	61.4	1.899	0.588	23.895	17.138	8.5	1.897	0.678	28.712	24.868	10.3	2.375	0.888	23.776	25.417	23.7	26.0
GeoTrans [28]	1.296	0.300	38.783	19.247	42.2	1.133	0.319	16.224	<u>5.267</u>	<u>68.7</u>	<u>1.183</u>	<u>0.375</u>	5.524	2.217	80.5	1.037	0.514	8.639	3.235	85.6	69.3
BUFFER [2]	<u>1.119</u>	<u>0.182</u>	8.679	<u>1.893</u>	<u>81.6</u>	2.202	0.435	36.861	12.615	30.2	2.747	0.556	70.534	27.838	3.2	-	-	76.648	39.030	0.0	28.8
PARE [38]	4.022	1.383	62.691	43.978	0.4	<u>0.951</u>	<u>0.293</u>	63.597	23.863	0.4	3.275	0.329	66.382	18.167	1.1	1.695	0.685	46.054	16.752	25.2	27.1
UGP (Ours)	0.384	0.117	0.749	0.263	98.6	0.794	0.249	3.652	1.613	89.7	1.139	0.378	<u>13.235</u>	<u>5.616</u>	<u>78.9</u>	<u>1.385</u>	0.596	<u>17.767</u>	<u>8.927</u>	<u>71.9</u>	84.8

Table 6. Cross-distance generalization experiments. We train at KITTI@40m and then test at 40m and nearer distances at 10m, 20m, and 30m. RRE and RTE denote the error for successfully matched point cloud pairs, while RRE* and RTE* reflect the error for all point cloud pairs, providing a more comprehensive evaluation. The final column shows the mean Registration Recall.

Model	Train on KITTI@10m					KITTI@20m					KITTI@30m					KITTI@40m					mRR
	RRE	RTE	RRE*	RTE*	RR	RRE	RTE	RRE*	RTE*	RR	RRE	RTE	RRE*	RTE*	RR	RRE	RTE	RRE*	RTE*	RR	
CoFiNet [39]	0.699	0.175	1.912	0.731	94.2	1.739	0.488	9.901	8.917	46.6	1.934	0.878	<u>22.910</u>	28.894	1.1	-	-	<u>24.768</u>	39.194	0.0	35.5
GeoTrans [28]	0.291	0.082	0.358	0.095	99.3	2.453	0.815	36.227	26.501	2.1	4.298	1.232	44.197	35.805	0.5	2.229	0.855	48.724	45.975	1.4	25.8
BUFFER [2]	0.309	<u>0.091</u>	0.311	<u>0.097</u>	99.8	<u>0.645</u>	<u>0.188</u>	<u>2.988</u>	<u>1.554</u>	<u>92.5</u>	<u>0.997</u>	0.291	24.145	<u>15.086</u>	<u>51.4</u>	<u>1.511</u>	0.445	45.820	<u>30.337</u>	<u>20.1</u>	<u>66.0</u>
UGP (Ours)	<u>0.296</u>	0.093	<u>0.336</u>	0.110	<u>99.5</u>	0.488	0.170	0.615	0.274	97.5	0.816	<u>0.354</u>	5.348	1.879	90.3	1.091	<u>0.527</u>	19.566	11.560	66.9	88.6

Table 7. Cross-distance generalization experiments on KITTI-Sparse. We train at KITTI@10m and then test at KITTI-Sparse@10m and farther distances at KITTI-Sparse@20m, KITTI-Sparse@30m, and KITTI-Sparse@40m. KITTI-Sparse denotes that we use farthest point sampling (FPS) to downsample the input point clouds to 5000 points. RRE and RTE denote the error for successfully matched point cloud pairs, while RRE* and RTE* reflect the error for all point cloud pairs, providing a more comprehensive evaluation. The final column shows the mean Registration Recall.

where M is the number of point cloud pairs to be aligned.

9. Additional Experiments

9.1. Cross-distance (train on KITTI@40m)

To comprehensively evaluate the generalization across different distances, we train on long-distance data (KITTI@40m) and generalize to shorter distances, as shown in Tab. 6. The results reveal that methods such as FCGF [8], Predator [16], CoFiNet [39], BUFFER [2], and PARE [38] struggle to achieve direct convergence at long distances. In contrast, the GeoTrans [28] network demonstrates the ability to converge at long distances and deliver good performance. However, its performance drops significantly when applied to simpler scenarios, such as KITTI@10m and KITTI@20m. This suggests that GeoTrans heavily relies on the visible data distribution, further highlighting that its cross-attention mechanism fails to adapt to variations in consistency representation of the same structure across different distances and datasets. Consequently, it cannot learn robust and generalizable features for LiDAR scenes. In contrast, our method not only successfully converges on KITTI@40m, but also gradually improves its performance as the distance decreases, consistent with the expected difficulty of the registration task. Ultimately, our method UGP achieves an mRR of 84.8%, which is 15.5% significantly ahead of the suboptimal GeoTrans.

9.2. Cross-dataset (KITTI@10m to Waymo@10m)

To comprehensively evaluate the cross-dataset generalization ability of our method, we supplemented the results with

Model	Waymo@10m				
	RRE(°)	RTE(m)	RRE*(°)	RTE*(m)	RR(%)
FCGF [8]	0.137	0.081	0.597	0.155	<u>99.2</u>
SpinNet [1]	0.377	0.096	0.553	0.171	<u>99.2</u>
Predator [16]	0.190	0.082	0.190	0.082	100.0
CoFiNet [39]	0.179	<u>0.080</u>	0.179	<u>0.080</u>	100.0
GeoTrans [28]	0.255	0.124	3.740	7.247	61.5
Buffer [2]	<u>0.171</u>	0.088	<u>0.171</u>	0.088	100.0
PARE [38]	0.270	0.136	1.051	4.003	76.9
UGP (Ours)	0.137	0.075	0.137	0.075	100.0

Table 8. The results of the cross-dataset generalization experiments from KITTI@10m to Waymo@10m.

training on KITTI@10m and testing on Waymo@10m. For the Waymo dataset (64-line LiDAR), we follow the same protocol in [31] and utilize the testing subset, the results are shown in Tab. 8. Our method achieved a state-of-the-art RR of 100% and the lowest errors in both RRE and RTE.

9.3. KITTI-Sparse

To evaluate the robustness of the network to extremely sparse LiDAR point clouds, we use farthest point sampling (FPS) to downsample the input point clouds to 5000 points, which is referred to as KITTI-Sparse. We compare CoFiNet [39], GeoTrans [28], and BUFFER [2], with the results shown in Tab. 7. UGP demonstrates a significant advantage at 20m, 30m, and 40m. Compared to the suboptimal BUFFER, UGP achieves 97.5% (+5.0%) RR at 20m, 90.3% (+38.9%) RR at 30m, and 66.9% (+46.8%) RR at 40m.

Noise σ	Method	Train on KITTI@10m					KITTI@20m					KITTI@30m					KITTI@40m					mRR
		RRE	RTE	RRE*	RTE*	RR	RRE	RTE	RRE*	RTE*	RR	RRE	RTE	RRE*	RTE*	RR	RRE	RTE	RRE*	RTE*	RR	
0.01	FCGF [8]	0.214	0.061	0.868	0.153	98.9	0.389	0.128	5.507	1.323	92.8	1.080	0.415	11.739	10.998	62.0	1.634	0.835	20.555	30.727	18.7	68.1
	BUFFER [2]	0.266	0.073	0.269	0.079	99.8	0.472	0.128	0.520	0.280	98.6	0.669	0.237	1.366	1.876	93.0	1.037	0.363	13.327	15.820	61.1	88.1
	UGP (ours)	0.243	0.071	0.294	0.078	99.8	0.399	0.144	0.441	0.219	99.3	0.641	0.282	2.206	1.052	95.7	0.994	0.478	12.938	7.174	78.4	93.3
0.03	FCGF [8]	0.204	0.060	0.908	0.158	98.7	0.374	0.117	6.149	1.731	91.4	1.014	0.396	11.600	11.886	58.2	1.648	0.728	22.072	31.061	17.9	66.6
	BUFFER [2]	0.277	0.074	0.278	0.080	99.8	0.478	0.127	0.508	0.342	98.6	0.720	0.243	3.293	2.026	93.0	0.959	0.358	18.489	17.286	55.4	86.7
	UGP (ours)	0.246	0.070	0.292	0.077	99.8	0.419	0.147	0.461	0.222	99.3	0.607	0.285	2.054	1.180	95.7	0.880	0.451	16.181	6.449	77.0	93.0
0.05	FCGF [8]	0.216	0.061	1.205	0.235	98.6	0.422	0.130	5.774	1.839	91.0	1.248	0.410	11.973	14.004	53.3	1.601	1.004	19.855	31.803	17.0	65.0
	BUFFER [2]	0.287	0.073	0.289	0.080	99.8	0.496	0.129	0.544	0.280	98.6	0.790	0.252	3.491	2.286	91.9	1.119	0.397	18.584	17.225	51.8	85.5
	UGP (ours)	0.253	0.070	0.285	0.077	99.8	0.427	0.150	0.460	0.224	99.3	0.597	0.283	3.554	1.214	93.5	1.101	0.488	14.526	8.571	75.5	92.0

Table 9. **Comparison of results under varying noise intensities**, with σ representing the standard deviation. RRE and RTE denote the error for successfully matched point cloud pairs, while RRE* and RTE* reflect the error for all point cloud pairs, providing a more comprehensive evaluation. The final column shows the mean Registration Recall.

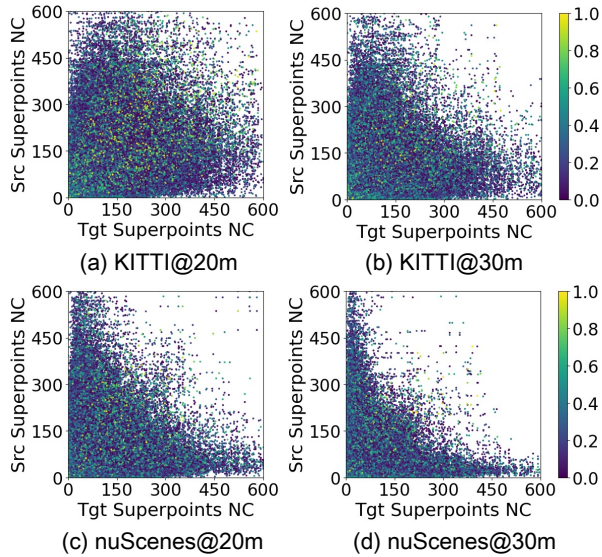


Figure 7. **Visualization of data distributions for ground truth matching point pairs across varying distances and datasets.** (a-d) Each point in the figure represents a ground truth corresponding superpoint pair. The position of each point indicates the neighborhood count (NC) of the superpoint within a radius of $r = 2.4m$ in both the source (src) and target (tgt) point clouds, and the color represents the overlap degree of the corresponding superpoint pairs after rotation by the ground truth transformation.

9.4. KITTI-Noise

To evaluate the robustness of our method to noise in real-world environments, we add Gaussian-distributed random noise $N(0, \sigma^2)$ (clipped to $[-3\sigma, +3\sigma]$) to each point’s position to simulate the measurement errors and noise encountered by LiDAR sensors in real-world scenarios, as shown in Tab. 9. Since other methods almost completely fail at long ranges, we only compare our method with FCGF [8] and BUFFER [2]. Our method achieves the highest RR across different levels of noise. Notably, the RR of our method remains unaffected at short distances, such as KITTI@10m and KITTI@20m. At KITTI@30m, the

RR decreases by 3.3% under a noise level of $\sigma = 0.05$. At KITTI@40m, the decrease reaches 6.5% under the same noise level. In summary, our method experiences an mRR reduction of no more than 2.5% (from 94.5% to 92.0%) at an intensity of $\sigma = 0.05$, demonstrating a certain level of robustness to noise.

LayerNum	KITTI@30m (RR%)	KITTI@40m (RR%)
2	95.1	<u>80.6</u>
3	96.8	82.0
4	95.7	74.8
5	<u>96.2</u>	72.7
6	95.7	72.7

Table 10. **Ablation experiment** of progressive self-attention module partitioning **with different number of spatial layers L** . $L = 3$ is selected to achieve the highest RR on KITTI@30m and KITTI@40m.

9.5. Ablation of Parameter

We conducted an ablation study on the number of layers L used to divide the space in the PSA. As shown in Tab. 10, we selected $L = 3$, which provided the best performance, as the final network implementation.

9.6. Mechanism Analysis

Admittedly, cross-attention achieves promising performance under same-distance/dataset settings. However, for LiDAR registration requiring cross-domain generalization, we identify a fundamental limitation: Cross-attention learns static density matching patterns from training data but struggles to extrapolate to the real physical law of LiDAR density decay ($\rho \propto 1/d^2$). When applied to cross-distance or cross-dataset scenarios, the learned correlation patterns become invalid due to density scaling or differences in LiDAR type.

To this end, we analyzed the $\text{Softmax}(QK^T/\sqrt{d})$ mechanism in UGP w. cross-attention, as shown in Fig. 8. At K@10m training, regions with high cross-attention scores (Top-10) covered 91.64% of true matches, *validating the effectiveness of the QK^T mechanism in capturing*

point cloud correspondences and guiding feature updates. However, cross-distance or cross-dataset scenarios exhibit LiDAR distribution shifts, causing true matches in high-score regions to plummet. This introduces false matches, increases feature ambiguity, and weakens generalization.

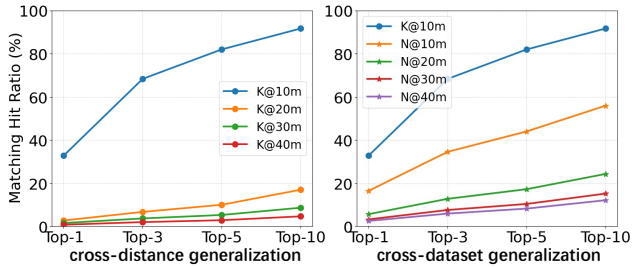


Figure 8. Visualization of the matching hit ratio in cross-distance and cross-dataset generalization experiments.

10. Visualizations

LiDAR Point Cloud Registration Characteristics. To supplement Fig. 2 (a) in Sec. 3, we provide additional details. Specifically, Fig. 7 illustrates the data distributions of ground truth matching point pairs for KITTI and nuScenes at distances of 20m and 30m.

Registration Results. The cross-distance registration results for KITTI and nuScenes are shown in Fig. 9 and Fig. 10.

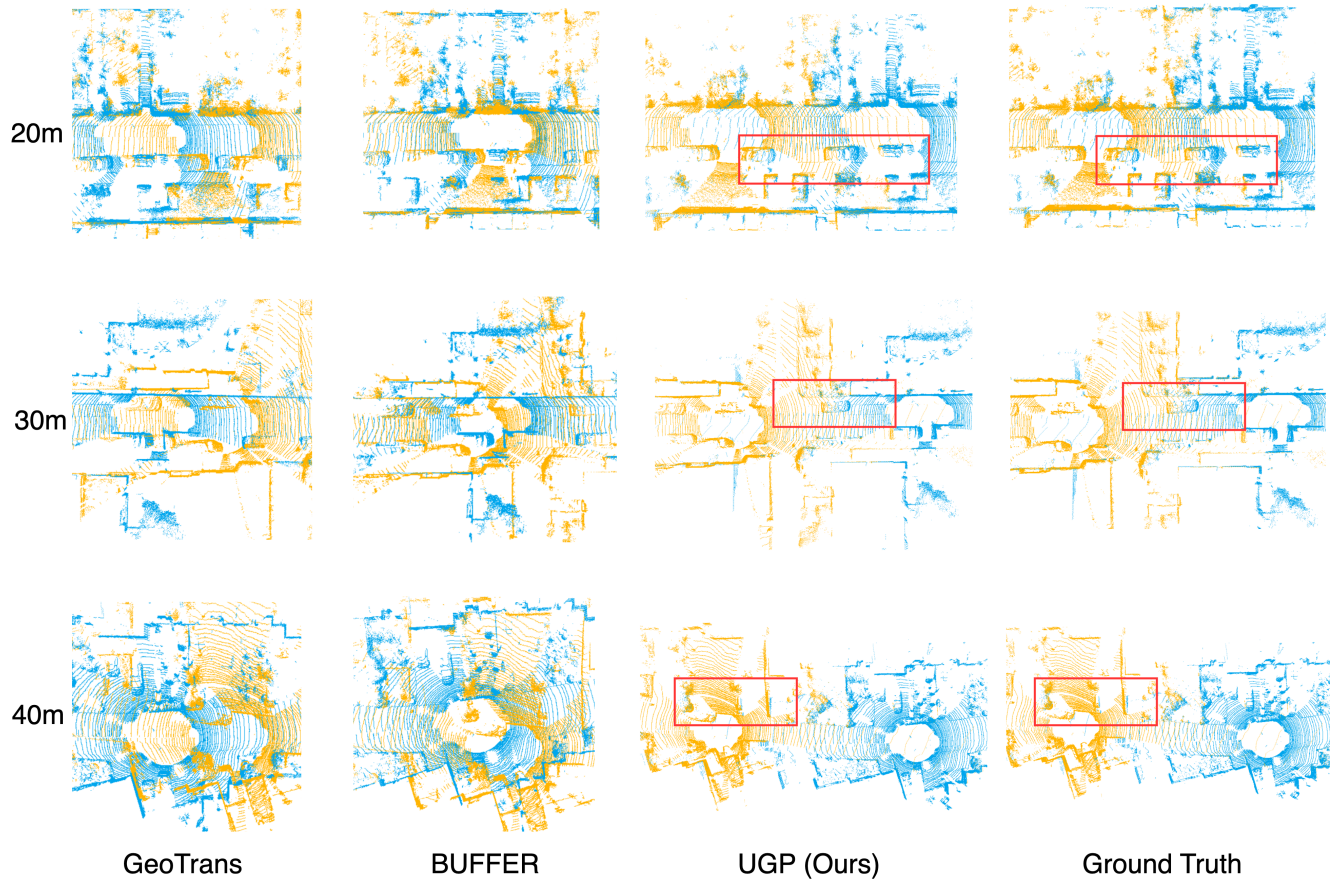


Figure 9. **Cross-distance generalization visualization** of GeoTrans [28], BUFFER [2], and UGP on the KITTI [12] dataset. Each row shows the point cloud pair matching results at different distances.

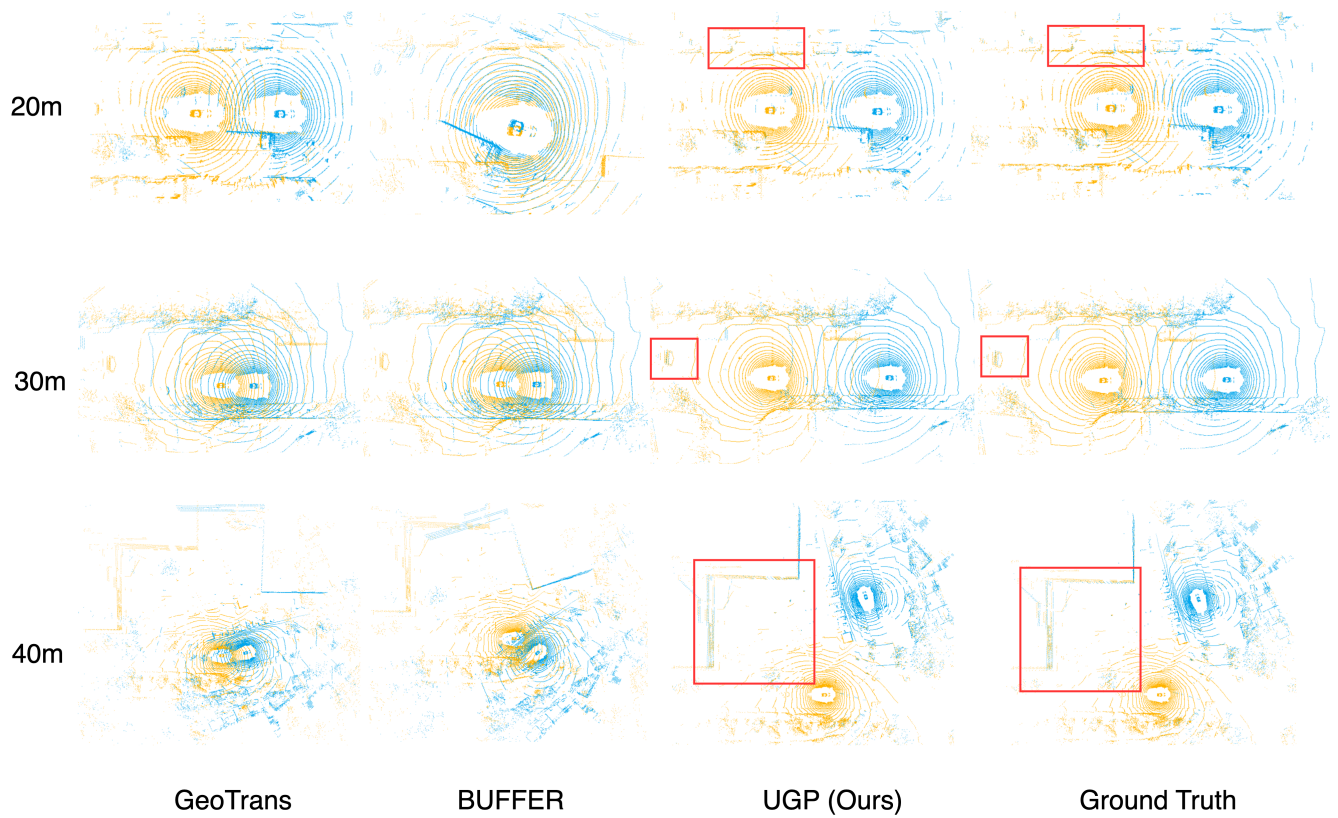


Figure 10. **Cross-distance generalization visualization** of GeoTrans [28], BUFFER [2], and UGP on the nuScenes [4] dataset. Each row presents the point cloud pair matching results at different distances.